SiO Molecular Jets around young stars - A numerical perspective

B. Vaidya[1]⋆, Tom Douglas[1], Paola Caselli[1]
[1]*School of Physics and Astronomy, University of Leeds, Leeds LS2 9JT*

4 October 2013

ABSTRACT
A bipolar, violent, collimated outflow is one of the first signposts of star formation. Such an outflow is believed to be launched magnetically from underlying accretion disk. As it propagates through the molecular cloud, it injects energy and momentum via shocks and fosters chemical evolution by forming, destroying and entraining molecules along its path. High velocity molecular outflows are extensively studied for both low mass and high mass stars. They are usually observed using standard sub-mm outflow and shocks tracers like CO and SiO respectively. However, the exact nature of the excitation of these molecules is not yet clear due to lack of models that simultaneously study the dynamics along with complex molecular chemistry. For such a study, we have performed MHD simulations of knotty jet propagation into a molecular cloud using the PLUTO code. Firstly, we evolve the jet dynamical quantities in conjunction with different non-equilibrium cooling prescriptions of varying complexities. The most complex is that of molecular cooling along with H_2 chemistry. This prescription allows us to track the formation and destruction of HI, HII and H_2 along with the flow dynamics. The final state of the jet obtained for each cooling model is then post-processed using a radiative line transfer code to obtain SiO emission maps, spectra and PV digrams. Our model can successfully explain the signatures of extremely high velocity (EHV) emission of SiO seen in early outflows. In particular, the line intensities, spectra and PV diagrams obtained from our model are very similar to that observed in case of outflows with EHV emission. In addition, the ALMA predictions for such early molecular outflows shows bright emission coming from young internal knots and primary bow shock due to thermal instability. Our multi-line modeling of SiO support the observational feature for example seen in Herbig-Haro (HH211) that higher line transitions trace regions close to the axis of the jet. The dependence of emission on different cooling prescription and abundance profiles is clearly outlined from our parameter study.

Key words: MHD – methods:numerical – ISM: jets and outflows

1 INTRODUCTION

Jets are one of the first manifestations of star formation in dense molecular cores. They are ubiquitous in both massive and low mass star forming regions. These supersonic flows, perpendicular to the underlying accretion disk, play a vital role in removing excess angular momentum and thereby aiding in the accretion onto the protostar. For low mass stars, they are believed to be launched by magneto-centrifugally forces and further collimated by magnetic hoop stress (Blandford & Payne 1982; Konigl & Pudritz 2000). However, in case of high mass stars, radiative forces also

contribute to flow dynamics during the later evolutionary stages Vaidya et al. (2011). Typically, these jets are few parsec in size long and can be divided into three length-scale domains viz. source and disk scales (1-10^2 AU), envelope scales ($10^2 - 10^5$ AU) and parent cloud scales ($10^5 - 10^6$ AU) REFERENCE. Of these, it is at the envelope scale where rich chemical evolution occurs as the jet interacts with the molecular medium. In this region, the jet propagates into a relatively static medium inducing shocks that are interesting from both a physical and chemical point of view. In addition to shocks, molecular material from the surroundings is entrained and accelerated to high velocities giving rise to molecular outflows.

Bipolar molecular outflows from low and high mass

stars have been studied in detail over the past decade (see reviews by Bachiller 1996; Arce et al. 2007; Tafalla & Bachiller 2011). Advances in millimeter interferometer allow observations of these outflows with spatial resolution of few arc seconds. A large number of studies observing young outflows are done using standard outflow and shock tracers, e.g. CO and SiO respectively. In addition to these molecular tracers, shocks from these outflows are detected in molecular hydrogen using infra-red telescopes. Also, energetic outflows like that of Orion source I show evidence of SiO masers very close to the launching region of a MHD disk wind (Goddi et al. 2009; Vaidya & Goddi 2013). Based on these observational studies, various empirical properties for these outflows have been discovered. For example, the CO outflows from single dish studies are seen to be highly collimated for both low and high mass stars (for e.g., Gueth & Guilloteau 1999; Beuther et al. 2002) they are referred to as *molecular jets*. These outflows also exhibit a mass-velocity relation with a power law form $dM(v)/dv \propto v^{-\gamma}$, where values of γ range from 1 to 3 Downes & Cabrit (2003). Episodic knots believed to be caused by variable accretion events are a common property of young molecular outflows (for e.g. in L1577: Gueth et al. 1998, in HH300: Arce & Goodman 2001a). These knots show their signatures as *wedges* in the position-velocity (PV) diagrams Arce & Goodman (2001b). Also, most commonly observed in these outflows are signatures of rotation and precision (for e.g., in DG Tau: Bacciotti et al. 2002).

Even with a myriad of such empirical evidence, the exact nature of these SiO and CO outflows is not clear. For a complete understanding it is imperative to compliment these observations with theoretical models. Many models based on hydro-simulations and steady state shock calculations were proposed to explain the observational signatures of molecular outflows. Among them the two main models are that of wide-angled wind driven Shu et al. (1991) and jet driven outflow Canto & Raga (1991). The most popular among them is the jet driven model as wind driven molecular outflows not only fail to match observed PV diagrams Cabrit & Bertout (1992) but also tend to sweep large quantity of material at the extremities of the lobes Masson & Chernin (1992). While the jet driven models could successfully derive the global outflow shapes and mass velocity relations of CO outflows (Raga & Cabrit 1993; Masson & Chernin 1993) . There have also been some attempts to combine these two models into one Shang et al. (2006) to explain the global observational features. However, most of these dynamical models do not account for shock chemistry. Instead, shock chemistry is studied independently using steady state non-dissociative C-type and dissociative J-type shocks models (Neufeld & Dalgarno 1989a; Schilke et al. 1997; Flower et al. 2003). The magneto-hydrodynamic (MHD) calculations by Glassgold et al. (1991) suggested that molecules like SiO and CO could form within the jet. Similar conclusions of molecules surviving in steady state disk winds have also been shown Panoglou et al. (2012). Very few simulations have modelled the outflow dynamics including molecular chemistry but in absence of magnetic fields (Raga et al. 1995; Smith & Rosen 2003). Recent models have also incorporated infall from envelope (Rawlings et al. 2013) and radiation transfer (Offner et al. 2011) to explain molecular emission from Class 0 protostellar outflow sources.

In the present work, our goal is to take a step further in the modeling of jet driven molecular outflows. The present model aims to consistently derive observed emission properties of molecular outflows, specifically various SiO line transitions, by combining axisymmetric MHD simulations of radiative jet propagation with time-dependent chemistry and 3D radiative transfer. In particular, we evolve the jet dynamical quantities in conjunction with different non-equilibrium cooling prescriptions of varying complexities. The most complex is that of molecular cooling along with hydrogen chemistry. This prescription allows us to track the formation and destruction of HI, HII and H_2 along with the flow dynamics. The final state of the jet obtained for each cooling model is then post-processed using a non-LTE line radiative transfer code to obtain emission maps, spectra and PV digrams. These emission maps are further processed using the Common Astronomy Software Applications package (CASA) to obtain synthetic ALMA images of the resultant molecular outflows.

In the next three sections we describe our numerical setup, cooling prescriptions and radiative transfer code respectively. In sections 5 and 6, we will present results from the parameter survey and the discussions along with predicted ALMA maps will be presented in sections 7 and 8, followed by conclusions in section 9

2 NUMERICAL SETUP

2.1 Numerical code and Equations

For our study, we carry out numerical axisymmetric ideal MHD simulations using the PLUTO code (Mignone et al. 2007) which is based on a conservative scheme of Godunov type. We have modified the original code to incorporate molecular cooling from self-consistent evolution of hydrogen chemistry (see Sect. 3).

In general, the MHD code considers the following set of equations. The conservation of the mass and the momentum,

$$\frac{\partial \rho}{\partial t} + (\vec{v} \cdot \nabla)\rho + \rho \nabla \cdot \vec{v} = 0 \tag{1}$$

$$\rho(\frac{\partial \vec{v}}{\partial t} + (\vec{v} \cdot \nabla)\vec{v}) = -\nabla P + \frac{1}{4\pi}(\nabla \times \vec{B}) \times \vec{B} \tag{2}$$

where ρ is gas density, $\vec{v}$ the velocity vector, P the gas pressure, and $\vec{B}$ the magnetic field vector with the poloidal and toroidal components - $\vec{B}_{\rm p}$, B_ϕ. Note that the forces due to gravity are neglected for this problem as the domain of interest is far away from the central object.

The cooling function Λ which depends on temperature T, mass density ρ and chemical abundances $\mathbf{X}$, appears in the energy equation as a source term,

$$\frac{\partial}{\partial t}(\rho E) + \nabla \cdot \left[\rho E \vec{v} + (P + \frac{B^2}{8\pi})\vec{v}\right] - \vec{B}(\vec{v} \cdot \vec{B}) = -\Lambda(\rho, T, \mathbf{X}), \tag{3}$$

where the total energy density of the flow E comprises contributions from the internal energy ϵ, the mechanical energy and the magnetic energy,

$$E = \epsilon + \frac{v^2}{2} + \frac{B^2}{8\pi\rho}. \tag{4}$$

The gas pressure in the flow is related to the density assuming an equation of state with the adiabatic index γ,

$$P = (\gamma - 1)\rho\epsilon. \tag{5}$$

The evolution of chemical abundances for each species is solved via,

$$\frac{\partial \rho \mathbf{X}_i}{\partial t} + \nabla \cdot (\rho \mathbf{X}_i \vec{v}) = \rho \mathbf{S}_i, \tag{6}$$

where $\mathbf{S}_i$ represents the net creation or destruction of a given species through chemical reactions (see Sect. 3).

The evolution of the magnetic field is governed by induction equation,

$$\frac{\partial \vec{B}}{\partial t} = \nabla \times \left(\vec{v} \times \vec{B} \right). \tag{7}$$

In addition to the above set of equations the code obeys the condition of divergence-free magnetic fields, $\nabla \cdot \vec{B} = 0$, which is numerically achieved by construction using the Powell's eight wave formulation (Powell et al. 1999).

2.2 Initial Condition

We model the propagation of jet as it interacts with the molecular cloud core at distances great enough so the the central object no longer has significant impact on the evolution of the outflow, i.e. $\gtrsim 1000$ AU. At these distances from the central source, the downward pull of gravity plays a negligible role and the dynamics of the jet is primarily governed by magnetic fields. The total magnetic field in the jet is dominated by the toroidal component. This is because the poloidal field decays as z^{-2} as compared to z^{-1} for toroidal field to maintain the force balance (z is the vertical distance from source). The hoop stress due to pinch force from the toroidal magnetic fields maintains a highly collimated beam like structure for the jet.

The ambient medium with which the jet interacts primarily represents the molecular cloud core. The numerical domain is axi-symmetric and in (r,z,ϕ) cylindrical coordinates. Its extent 20 $R_{\rm j}$ in the radial direction and 100 $R_{\rm j}$ along the vertical axis ($R_{\rm j}$ being the radius of the jet). The domain of interest is about 3000 AU away from the central source and extends up to 0.1 pc. Numerically, it is resolved by an uniform grid with a domain of 200×1000 cells in the radial and vertical directions. For simplicity, we choose this medium to be unmagnetized and non-turbulent. The density in the ambient medium varies with vertical height z as, $\rho_{\rm amb} \sim (\rho_0/z^2)$ which is consistent with observations (Caselli 2011). The value of ρ_0 depends upon the density contrast, η, between the jet and the ambient medium. The number density in the jet is kept fixed such that the density in the ambient medium lies within a range of $10^4 - 10^5 {\rm cm}^{-3}$. The pressure in the ambient molecular medium is set so to maintain a constant temperature of 50 K.

The jet enters into the medium through a nozzle of radius $R_{\rm jet}$ from the lower boundary (z = 0). The jet density is fixed to be $10^5 {\rm cm}^{-3}$ and it has a radius of $2.5 \times 10^{15}{\rm cm} \sim 167$ AU. The jet is injected into the domain with a typical velocity of $v_{\rm jet,0} = 100$ km/s as is the case for most low mass stellar jets especially the low velocity component. The constant jet velocity is superimposed with periodic pulsation of the form,

$$v_{\rm jet} = v_{\rm jet,0}(1.0 + A\,sin(2.0\pi t/T_{\rm p})) \tag{8}$$

where the amplitude A is 0.25 and time period $T_{\rm p} = 70$ years. The pressure at the surface of the jet is $10^{-10}{\rm dyne\ cm}^{-2}$ corresponding to a temperature of $T_{\rm jet} \sim 4 \times 10^3\,K$. Inside the jet beam, a radial variation of thermal and magnetic pressure is adopted to maintain a magneto-static equilibrium. We adopt the same radial profiles used by Stone & Hardee (2000) for all our runs. Based on these profiles, the toroidal magnetic field is assumed to be zero at the axis and achieves a maximum at some radius, $r_{\rm m}$ inside the jet. The maximum value, $B_{\phi,\rm m}$, depends on the plasma β which is kept fixed for all our runs to be at a value of 10.0. This corresponds to the maximum field strength, $B_{\phi,\rm m} \sim 16\mu\,G$.

In order to consistently model the SiO emission arising from shocks as this jet interacts with the medium, we evolve the dynamics along with chemistry and cooling prescriptions. They are described in details in the next section.

3 CHEMISTRY AND COOLING

3.1 Molecular Cooling

Typically, early collimated outflows have cooling times shorter than the dynamical times, implying that the radiative cooling plays a vital role in dynamics. In order to study such outflows it is necessary to evolve the dynamics in conjunction with full molecular chemistry and associated radiative processes. However, evolving a full complex network of chemical equations along with dynamics is a very computationally intensive task. As a result, we have focused only in evolving the chemical equations pertaining to atomic and molecular hydrogen. This prescription of molecular cooling has been added to the PLUTO code to study the chemical evolution of molecular outflows during the very early phases of star formation. In particular, the total hydrogen number density n_H comprises of contribution from atomic and molecular hydrogen i.e., $n_H = n_{HI} + n_{H2}$. Whereas the contribution to electrons comes from the ionized hydrogen, n_{HII} and from negligible but fixed fraction of metals ($Z \sim 10^{-4}$). The chemical evolution of molecular, atomic and ionized hydrogen is governed by equations listed in Table 1.

Numerically, the non-homogenous parts of the equations 3 and 6 are are solved separately from the advection step using operator splitting. Further, the rate equations are evolved at each advection time step using sub-stepping and adaptive Runge-Kutta methods. In doing so, the code tracks the formation and destruction of fractions of three species viz., X(HI), X(H_2) and X(HII) based on the temperature dependent reaction rates specified in the table along with their references and shown in the left panel of figure 3.1. The figure clearly shows that below 1000 K the formation of molecular hydrogen dominates over other chemical processes, whereas for hotter gas there exists a competition of different chemical processes elucidating the complex chemical interplay. The fractions of various hydrogen species are then used to update the cooling function $\Lambda(\rho, T, \mathbf{X})$ to consistently derive the temperature for next advection step. For low temperatures, we also take into account contribution to cooling rates from molecules like CO, whose abundance with respect to $n_{\rm H2}$ is fixed to 10^{-5}. For each of the other molecules contributing to the cooling function (like OH, H_2O
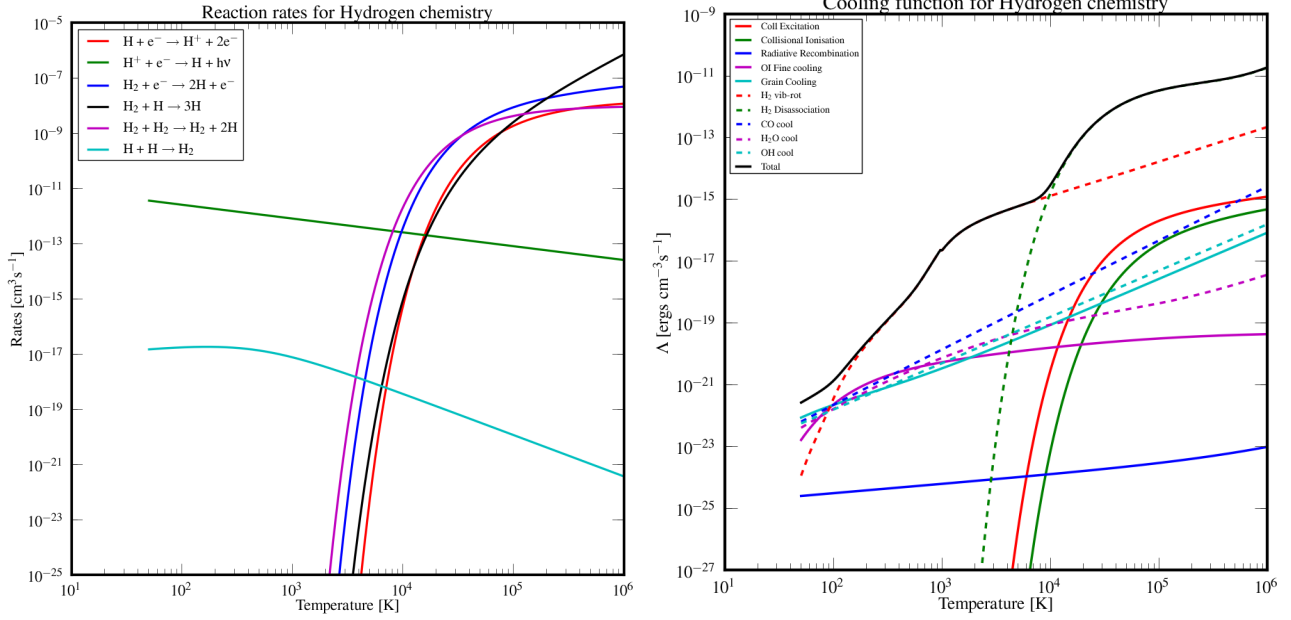
Figure 1. Variation of H_2 chemistry reaction rates, k_i and cooling function $\Lambda(n, T, \mathbf{X})$ with temperature for the initial state (see Sect. 3.1)

Table 1. Summary of the chemistry reaction set. T is the temperature in Kelvin, T_{eV} is the temperature in electron-volts, $T_5 = T/1 \times 10^5$ and $T_2 = $ T/100

No.	Reaction	Rate Coefficient ($cm^3 s^{-1}$)	Reference [a]
1.	$H + e^- \rightarrow H^+ + 2e^-$	$k_1 = 5.85 \times 10^{-11} T^{0.5} \exp(\text{-157,809.1/T})/(1.0 + T_5^{0.5})$	1
2.	$H^+ + e^- \rightarrow H + h\nu$	$k_2 = 3.5 \times 10^{-12}(T/300.0)^{-0.8}$	2
3.	$H_2 + e^- \rightarrow 2H + e^-$	$k_3 = 4.4 \times 10^{-10} T^{0.35} \exp(-102,000.0/T)$	3
4.	$H_2 + H \rightarrow 3H$	$k_4 = 1.067 \times 10^{-10} T_{eV}^{2.012}(\exp(4.463/T_{eV})^{-1}((1. + 0.2472 T_{eV})^{3.512})^{-1}$	4
5.	$H_2 + H_2 \rightarrow H_2 + 2H$	$k_5 = 1.0 \times 10^{-8} \exp(-84,100/T)$	2
6.	$H + H \xrightarrow{dust} H_2$	$k_6 = 3.0 \times 10^{-17} \sqrt{T_2}(1.0 + 0.4\sqrt{T_2 + 0.15} + 0.2 T_2 + 0.8 T_2^2)$	5

[a] REFERENCES – (1) Cen (1992) [Eq. 26a]; (2) Woodall et al. (2007) [UMIST Database] (3) Galli & Palla (1998) [Eq. H17]; (4) Abel et al. (1997) [Tab. 3 Eq. 13]; (5) Hollenbach & McKee (1979) [Eq. 3.8]

and atomic OI) the abundance is fixed to 5×10^{-6}. The contribution from these molecules is only important when temperature is < 100 K as seen in the right panel of figure 3.1.

3.2 Additional Cooling Prescriptions

For comparison, we also ran simulations of axisymmetric MHD jets with optically thin cooling prescriptions already existing in the public release of the PLUTO-4 code. They are power-law cooling, simplified non-equilibrium (or atomic) cooling and tabulated cooling. Further we compare these radiative runs with an adiabatic jet to cover a wide spectrum of jet thermodynamics.

In case of power law cooling, the radiative losses denoted by $\Lambda(\rho, T, \mathbf{X})$ are proportional to $\rho^2 T^\alpha$, with $\alpha = 0.5$ representing bremsstrahlung cooling. The loss term is independent of the fraction of various species $\mathbf{X}$, therefore the fluid density ρ is assumed to be all hydrogen for further processing of emission maps. Similarly, for tabulated cooling prescription, the radiative losses are estimated based on

a fixed fraction of various species. However, the contribution for each species is a complex function of density and temperature. The variation of cooling function Λ with temperature is shown in the right panel of figure 1. The formulations which depend on the fractions of each species and gas temperature of these variations are mainly adopted from the appendix of Smith & Rosen (2003). The fractions of all hydrogen species are kept fixed to their initial values, while that of CO, OH, H_2O and OI are same as that used for molecular cooling described above. The total cooling curve shown as the black solid line in the figure 1 is used for the case of tabulated cooling. For the atomic cooling, we distinguish between neutral and ionized gas by defining $f_n = n_{HI}/n_H$ and evolve it using,

$$\frac{\partial f_n}{\partial t} + \mathbf{v} \cdot \nabla f_n = n_e[-(c_r + c_i)f_n + c_r] \qquad (9)$$

where, n_e is the number of electrons that come from ionized hydrogen and a very small fixed fraction of metals, c_r and c_i are the recombination and ionization rate coefficients that

depend on the temperature T. In addition to losses by collisional ionization and radiative recombination, additional contribution to radiative losses come from various atomic line emissions from C,N,O,Mg,Si,Fe etc.

While these additional cooling prescriptions may not be a complete description of the chemical and radiative processes in early outflows, they are ideal to compare the results obtained from the more consistent newly added molecular cooling. Such a comparison is presented in section 6.1.

4 RADIATIVE TRANSFER

4.1 The radiative transfer code

The radiative transfer program used is LIME (LIne Modeling Engine; Brinch & Hogerheijde 2010), which calculates line intensities based on a weighted sample of randomly chosen points in a continuous 3D model. The method of selecting these points is given in section 4.2. At each of these points, the density of the main collision partner (equivalent amount of H_2, given by $n(H_2)+$ 0.5 $n(H)$, assuming that atomic Hydrogen has half the SiO collisional cross section of molecular hydrogen and that ionized Hydrogen does not collide with SiO), gas and dust temperatures, velocity, molecular abundances and unresolved turbulent velocity are specified. These points are then smoothed by Lloyd's algorithm (Lloyd 1982) in order to minimise the variation in distance between points whilst keeping the same underlying distribution. These points are then connected by Delaunay triangulation and it is between the points connected by this method that photon are allowed to propagate (fig. 2). The level populations of the selected molecules are calculated at each of these points from collisional and radiative (de)excitation and the local radiation field is calculated. This is repeated 20 times with the populations of each level converging towards a single value. This number of iterations is sufficient for the signal to noise ratio of the level populations (as defined in Brinch & Hogerheijde 2010) to exceed 1000 for 99% of the points, ensuring that the simulation has converged on a stable level population. After 20 iterations the model is ray-traced in order to produce synthetic brightness maps. The average of ten separate runs was taken to minimise the artefacts in the output images, resulting from the grid construction.

4.2 Grid construction

In order to construct the grid, candidate points are randomly selected from the volume to be simulated. These candidates then have their equivalent H_2 number density, and the number density of SiO, compared against those of a reference point in order to decide if the candidate point is to be used in the grid or not. Candidate grid points are selected at random in a cylindrical coordinate system that is linearly spaced in z and θ and logarithmically spaced in r. For each point to be selected, a random number α is drawn from the semi-open set $[0, 1)$ as a threshold. After selection of random coordinates, the H_2 density and SiO density at the candidate point (n and m, respectively) are compared against the densities of a reference point in the un-perturbed ambient medium multiplied by a factor of $\frac{4\eta}{5}$ (n_0 and m_0).
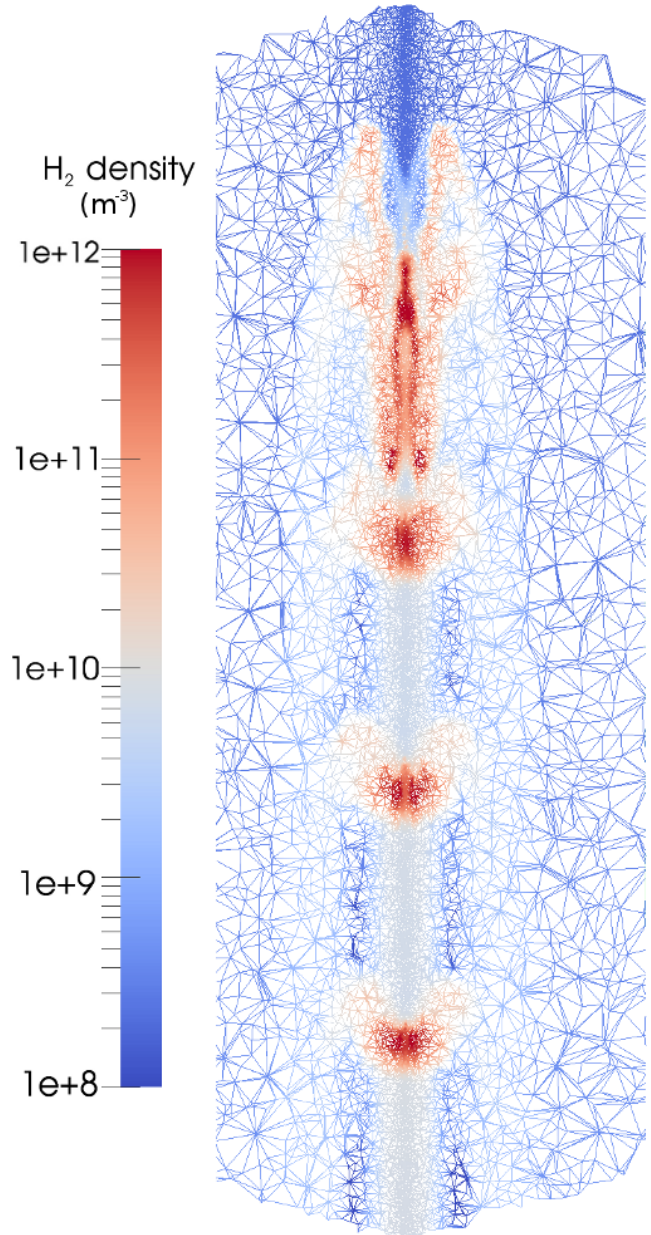
Figure 2. A plot of the points selected by the gridding process and the paths down which photons can propagate for points in the r,z plane. The points are color coded by the density distribution (in m^{-3}, as used in LIME) and are more concentrated in the high density knots.

If $\alpha < \left(\frac{n}{n_0}\right)^{0.3}$ or $\alpha < \left(\frac{m}{m_0}\right)^{0.3}$ then the point is selected for use. Otherwise another r, θ, z co-ordinate is selected and it becomes the candidate point. In addition to this method of selection, 5% of the points are linearly distributed in x, y and z with no bias with regards to density or abundance. This provides a minimum level of sampling for the large low density regions in the outer parts of the simulated volume.

4.3 SiO abundance

Molecular abundance is one of the important ingredients that is required by the radiative transfer code described

above. Typically, extremely low abundance of SiO is found $(n(SiO)/n(H2) < 3 \times 10^{-12})$ in dark, dense clouds such as TMC1 (Ziurys et al. 1989; Martin-Pintado et al. 1992). Whereas, in outflows like L1448, SiO abundance can increase up to 10^{-6} especially in molecular bullets moving with a projected velocity of $60 \, \mathrm{km \, s^{-1}}$ (Dutrey et al. 1997). Thus, there is a significant increase of 6 orders of magnitude from quiescent clouds to outflows crowded with shocks. Production of gaseous SiO due to slow C-type shocks has been suggested to occur via release of silicon from grain cores and from grain mantles. Various stationary shock models indicate a sudden abundance increase in SiO near a shock speed of 20-30 km s^{-1}. However, several young outflows have velocities of the order of 100 km s^{-1} as in the present case. Shocks due to such outflows will dissociate H_2 and will become J (*jump*) type shocks. Thus molecules observed in such energetic outflows must have been reformed in the flow as suggested by detailed models of J-shocks by Neufeld & Dalgarno (1989b). SiO formation in J shocks have also been modelled recently and have thought to be reasonable candidates of SiO line emission in molecular outflows and jets (Guillet et al. 2009).

In-spite of all numerical models relating to the study of enhancement of SiO in shocks, very little is known about the dependence of SiO abundance on shock speeds. Considering the complex grain chemistry that is involved in order to estimate the functional dependence of SiO abundance on shock speeds, we prescribe these profiles based on limited empirical evidences. The most simple among them is the top hat profile in which the SiO abundance is a low value of 10^{-12} below 20 km s^{-1} and above 100 km s^{-1} and a maximum value of 10^{-6} between these two velocities. In order to get rid of a discontinuous change of abundance, we also prescribe a gaussian such that the peak SiO abundance of 10^{-6} is at $60 \, \mathrm{km \, s^{-1}}$. While the value of $n(SiO)/n(H_2)$ falls below 10^{-9} at 20 and 100 km s^{-1}. These functional dependences of SiO abundance on shock velocity are show in figure 3. In addition to this if the temperature at the point is greater than $92,000 \, \mathrm{K}$ (the temperature of the Si-O bond disassociation energy) the abundance is reduced to 10^{-12}.

Further, the velocities obtained from the dynamical simulations are in fact the jet flow velocities. They can well be different from the shock velocities depending upon the density contrast between the jet and ambient medium. For the present study, we will consider two cases. Firstly, the most simple one in which the jet flow velocity is same as the shock velocity. Considering that there is a density contrast in the simulation setup this assumption is will overestimate the shock velocity. In order to correct the same we also consider a case in which the shock speed of a dense plug accumulated between the jet and medium is estimated by balancing the the respective ram pressures (Masson & Chernin 1993),

$$v_s = \frac{v_j}{1 + \eta^{-0.5}} = \frac{v_j}{\delta} \qquad (10)$$

where v_s is the velocity of dense plug and v_j is the jet velocity. A comparative view of using such velocity corrections and functional forms of SiO abundances are discussed in Sec 6.4.
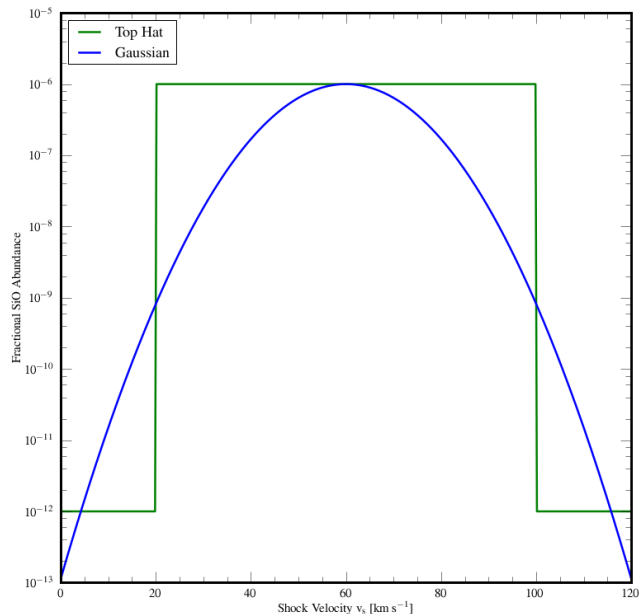
Figure 3. The different fractional SiO abundances as a function of shock velocity, v_s.

5 PARAMETER SURVEY

The results and analysis for the present work are divided in two parts, viz., the dynamical numerical simulations and the post-processing with radiative transfer code. For each part we have used certain parameters and the effect of changing them is studied. Ideally all these parameters should come from observational results. However, not all quantities needed for our study are well constrained by observations, thus allowing us vary them as free parameters. Such a parameter survey provides better handle on the range of allowed values on qualitative comparison with observations.

5.1 Parameter definitions

For the first part of the study concerning the dynamical numerical simulations, we will focus on two main parameters. They are the prescription of cooling and the density contrast between the jet and the ambient medium denoted by η. The various cooling prescriptions used for the present study are described in detail in section 3. They differ in the physical process that is responsible for cooling and chemistry. The most simple one is that of power-law cooling with no chemistry and the most complex cooling module is where molecular hydrogen chemistry is evolved with contributions to cooling from other abundant molecules like CO, OH etc.

A value of $\eta > 1$, means that that jet is over dense with respect to the medium. In all our runs with different cooling prescriptions, we have assumed the jet to be over-dense by 10 times that of the ambient medium. Additionally, for the atomic, tabulated and molecular cooling runs we have also used a value of η of the order of unity indicating similar densities in the jet and the medium. The magnetic field strength is kept to be fixed using $\beta = 10.0$, for all our runs. Table 2 lists all the runs with varying η and cooling prescriptions, along with the peak intensity and line widths at the bow shock.

To obtain the SiO emission maps and corresponding spectra, two additional free parameters are required along with other inputs described in section 4 . They are the fractional abundance profile of SiO and the angle of inclination with respect to line of sight denoted by ϕ. Section 4.3 describes all the profiles used for the present study. The obvious choice for the inclination angle, ϕ is $90°$ indicating the outflow is in the plane of the sky. Additionally, we have used two other angles of inclination apart from the plane of the sky, i.e, $\phi = 45°, 60°$ to compare results with observations. The runs with different fractional abundance profiles are described in table 3. A parameter introduced here is δ which is essentially the ratio of shock velocity v_s and physical jet velocity v_j such that its value depends on density contrast η (see Eq. 10).

5.2 Reference Run

We define a reference run in order to quantify and compare results obtained from such a survey of above mentioned parameters. The results shown in this work will be pertaining to the reference run and appropriate comparison will be discussed with other runs.

The reference run in our calculation has density contrast $\eta = 3$ with a plasma beta, $\beta = 10$. The jet for this run is 89% atomic, 10% molecular and 1% ionized to begin with. This jet enters the ambient medium with a velocity of $v_{jet,0}$ = 100 km s^{-1}. The cooling in the jet is via molecular cooling prescription, whereby the hydrogen fractions are evolved with cooling contributions for abundant molecules like CO, OH etc. The final state (at time $\sim$ 1000 yr) density, temperature and velocity obtained from this run is post-processed to obtain the observational features corresponding to SiO molecule. For the radiative transfer calculation, the source in the reference run is stationary and the jet is in plane of the sky ($\phi = 90°$). A gaussian profile is used for the fractional abundance of SiO. Further, the shock velocity which determines the fractional abundance, v_s, is less than the jet velocity in the flow, such that their ratio δ is given by $1./(1.0 + \eta(z)^{-0.5})$, where $\eta(z)$ is the density contrast as a function of height from the base of the jet, and is inversely proportional to the ambient density at the same height.

6 RESULTS

6.1 Comparison of cooling prescription

We have done a comparison study of jet dynamics with various cooling prescriptions, which are described in Sect. 3. Figure 4 shows the density of the MHD jet at time $\sim$ 1000 years for these different cooling prescriptions. For this study, we have chosen a density contrast at the base of $\eta = 10$ between the jet and ambient medium. It is clear from the figure, that the cooling plays a significant role in determining the structure of the jet. The jets with no or very little cooling are much wider compared to jets having dominant cooling. For example, the adiabatic jet has a widest bow shock at its apex and has the most prominent cocoon around it. While the jet with atomic cooling has a rather conical jet head with significantly less cocoon surrounding it. The cocoon is almost absent from the narrow jet with tabulated cooling.

Instead, the jet seems to form a very high density shell due to cooling of the processed ambient gas. Further, the jet with tabulated cooling is narrower than the jet with molecular cooling. This clearly shows the feedback of chemistry on the cooling function. The cooling terms for both these jets are the same to begin with, however, for the molecular jet the cooling terms evolve with jet dynamics as the fraction of various hydrogen species change over time. Whilst the terms remain fixed to initial values, shown in the right panel of fig 1, for the jet with tabulated cooling. Additionally, the material at primary bow shock for jet with tabulated and molecular cooling condenses forming dense knots. Such a condensation is caused due to thermal instability and is a typical feature of axi-symmetric radiative jets (see, for e.g, Blondin et al. 1990; Cerqueira & de Gouveia dal Pino 1999).

The dynamical states for each of this cooling prescription are then post-processed to obtain integrated J = 2->1 SiO emission maps shown in figure 5. The differences in dynamical features are also reflected in the corresponding SiO emission maps. These maps are obtained assuming an angle of inclination of $90°$ using the top hat abundance profile with $\delta = 1$. They are then placed at a distance of 100 pc and convolved with a beam with FWHM of 2.5″in order to create the maps shown. The emission features in jet with atomic and power-law cooling prescription do not have such a well defined lobe structure. For example, the emission from the jet with atomic cooling is mainly coming from regions close to R,Z = $\pm$ 10,80. In fact the emission from this region seems to be stronger than that coming from the conical jet head. In case of the jet with power-law cooling the emission seems to be mostly coming from the internal knots. The thin density layer formed at the interface of jet and the ambient medium do not show indication of any emission. The emission coming from jets with tabulated and molecular cooling show a distinctive outflow lobe which is typically observed in case of young molecular outflows. SiO emission coming from internal knots in these jets also show a distinctive turbulent pattern consistent with observations. Additionally, strong emission also comes from the condensation formed at the primary bow shock due to thermal instability.

In summary, different cooling prescriptions strongly influence the dynamics of MHD jet propagation in particular the thickness and structure of the primary bow shock. These dynamical differences are also reflected in SiO emission maps and spectra. Emission maps obtained from molecular cooling show a distinctive outflow lobe structure which is consistent with observations. The properties of molecular cooling flows are described in details in the next section.

6.2 Molecular cooling and H$_2$ Chemistry

In case of molecular outflows, the most appropriate form of cooling prescription among the ones described in sect. 3 is that which involves the evolution of H$_2$ chemistry along with contributions to cooling from fixed fractions of other molecules like CO, OH etc. First three panels of figure 6 show the density of various hydrogen species in the outflow for the simulation run with $\eta = 3$ and $\beta = 10$. The jet is largely dominated by atomic and molecular hydrogen, however, the fraction of these species have considerably changed from their initial values within the jet. Ionized hydrogen is

Table 2. Summary from parameter runs.

Run	Cooling Mode	η	Top Hat Profile $\delta = 1$		Gaussian Profile $\delta = 1$	
			$\int T_{\mathrm{MB}}dV$ [K-km s^{-1}]	Δv [km s^{-1}]	$\int T_{\mathrm{MB}}dV$ [K-km s^{-1}]	Δv [km s^{-1}]
adi1010	Nil (Adiabatic)	10	2.91	>40	0.25	40.0
pow1010	Power law	10	0.64	8.0	0.02	10.0
atm1010	Atomic	10	2.04	36.0	0.58	38.0
atm210	Atomic	2	3.21	18.0	0.64	20.0
tab1010	Tabulated	10	0.75	11.0	0.09	10.0
tab210	Tabulated	2	2.89	8.0	1.0	9.0
mol1010	Molecular	10	1.10	10.0	0.1	11.0
mol310	Molecular	3	3.3	14.0	0.66	12.0

Table 3. Summary of radiative transfer runs with different SiO fractional abundance profiles for dynamical simulation with molecular cooling and $\eta = 3$. The integrated intensity of the brightest lobe assuming a single disk observation with a beam width of 15$''$ is listed along with the corresponding spectral width.

Profile	$\delta = \mathrm{v_s/v_{jet}}$	$\int T_{\mathrm{MB}}dV$ [K-km s^{-1}]	Δv [km s^{-1}]
Top Hat	1.0	3.3	14.0
Top Hat	$1/(1.0 + \eta(z)^{-0.5})$	4.9	14.0
Gaussian	1.0	0.66	12.0
Gaussian	$1/(1.0 + \eta(z)^{-0.5})$	1.1	12.0
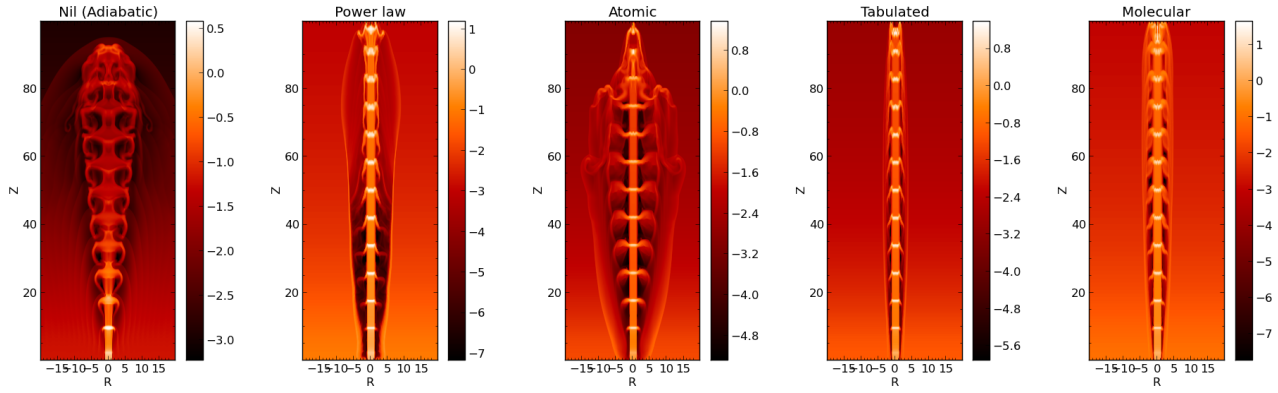
Figure 4. Jet Volume Density for different cooling modes with $\eta = 10$ and $\beta = 10$.
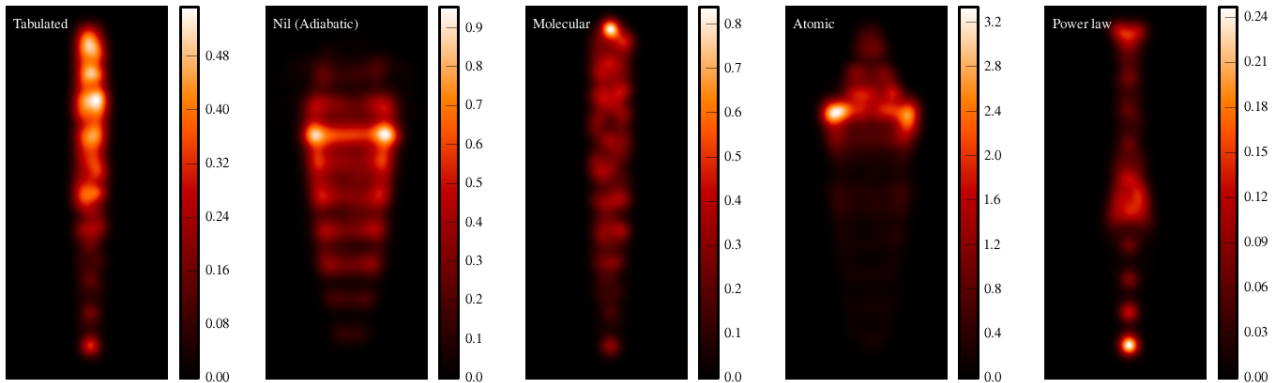
Figure 5. A plot of the integrated SiO J2-1 emission from 5 models, each using a different method to calculate cooling and all with η=10 β=10.

mainly formed at the tip of the bow as seen by the increase of fHII to 10% from an initial value of 1% within the jet.

The last two panels of figure 6 show the temperature and mean molecular weight μ. The highest temperature of ~ 50000 K is attained in our flow at the tip of the bow shock. While the temperature on the edges (i.e.,interface between jet and the ambient medium) is lower than 5000 K. Also the relatively weaker shocks formed due to knots do not heat up the material beyond few 10^3 K. The mean molecular weight, μ, gives an indication on which species of hydrogen dominates in each region of the flow. In particular, a value of $\mu > 2$. represents regions dominated by molecular hydrogen, while regions close to the bow shock have lowest values of μ where ionized hydrogen is present and along the jet the value μ is close to 1.3 suggesting an atomic jet.

The distribution of fractions of different hydrogen species along with temperature suggests that there are essentially three regions where chemistry is evolved due to shocks. They are : (1) The tip of the jet , (2) The edges of the jet and (3) intermediate knots. As the atomic jet propagates from the lower boundary into the cold molecular medium , it forms a strong shock resulting in forming a density and temperature discontinuity. Such a jump in dynamical quantities play a crucial role in evolution of chemistry. For example, temperatures beyond few 1000 K produced in the shocks could disassociate the molecules and can also lead to ionization if temperature reaches above 10^4 K.

For the reference run, the effect of shock in dynamical evolution of hydrogen fraction is presented in figure 7. The top panel of the figure shows number density of hydrogen in the jet. This hydrogen exists in three forms namely, molecular, atomic and ionized. The fraction of each of these forms are shown in bottom panels of figure 7 at two representative regions in the jet marked with the arrow. The left bottom panel shows the vertical distribution of temperature, molecular and atomic fraction at the interface of the knot and the ambient medium. The interaction of the knot with the medium raises that temperature to 1200 K and accumulates the matter such the density in that region reaches up to 10^6 cm^{-3}. Behind the shock as the material cools, atoms combine together to form molecules as seen in the increase of fH2 from 0.44 to 0.52. This rise in molecular fraction comes at an expense of reduction in atomic fraction from 0.56 to 0.48. Further away from the shock, these species tend to reach a quasi equilibrium as their fractions reach towards a value of 0.5. The ionized fraction is extremely low in this region due to low temperatures. However at the bow-shock, temperatures rise up to 20000 K. Molecular hydrogen species are destroyed, while ionized hydrogen shows an increase in its fraction as seen in the bottom right panel of figure 7. The peak in ionized fraction of 0.15 coincides with the peak in temperature profile as expected. The molecular fraction shows a considerable dip from 0.3 to 0.03 at this temperature before rising sharply in the ambient molecular medium.

In summary, the axi-symmetric jet flow with periodic knots produce shocks of varied strengths giving rise to density, velocity and temperature distribution. Molecular cooling and chemistry also allows us to evolve fractions of different hydrogen species along with the jet flow. These jet quantities are then post-processed with a radiative transfer code described in section 4 to obtain emission maps, spectra and PV diagrams.
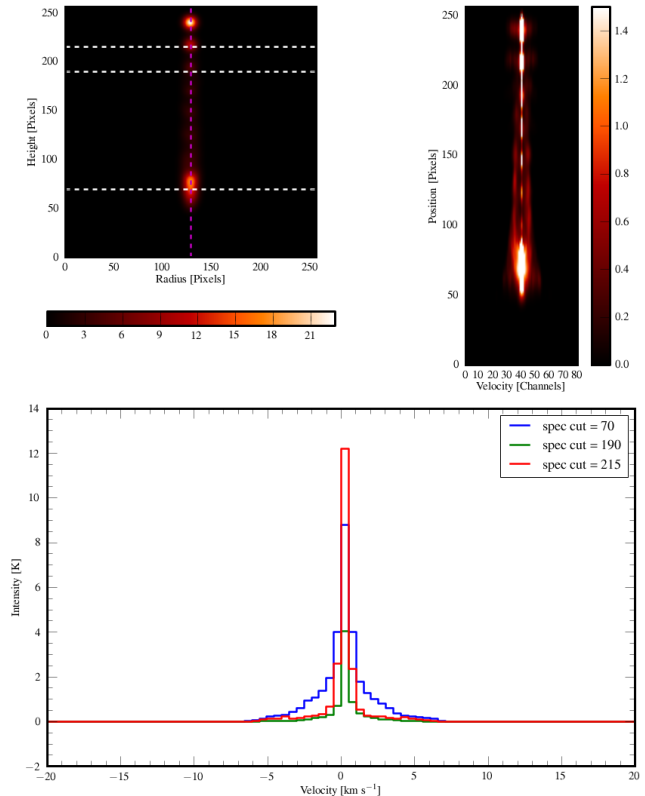

Figure 8. Integrated Emission map (*top left*), PV diagram (*top right* and spectra (*bottom* for the 2->1 SiO transition for the reference run. The jet is assumed to be in the plane of sky implying an angle of inclination of 90°. The vertical *magenta dashed* line represents the cut for the PV digram and where this line is intersected by the horizontal *white dashed* lines marks the positions from which the spectra are taken.

6.3   Emission Maps, Spectra and PV diagrams

The output obtained from the radiative transfer calculation is a data cube with velocity being the third axis. This allows us to obtain spectra and position velocity diagrams from these data cubes. Figure 8 shows all the possible outputs from the data cube for the J = 2->1 transition for the reference run. The top left panel in the figure shows the emission map for the jet directed downwards. The notable features are the knots close to the base of the jet and the emission near the bow shock due to density enhancement by cooling instability. The PV diagram shown in the top right panel is obtained along the jet as indicated by vertical magenta line. The position is shown in terms of pixels, where each pixel has a width of about 16 AU. The channel numbers in the X-axis indicate velocities. The whole velocity range of -20 km s^{-1} to 20 km s^{-1} is uniformly divided into 80 channels. High velocity features are clearly seen in regions corresponding to the knots in the emission maps. These features fade along the jet as the knots also disappear in the emission map. The region close to the bow shock as well gives indication of high velocity features which are seen as broad wings in the spectra.

The spectra at three different positions in the flow are shown in the bottom panel of figure 8. These three positions are basically the two knots close to the base of the flow
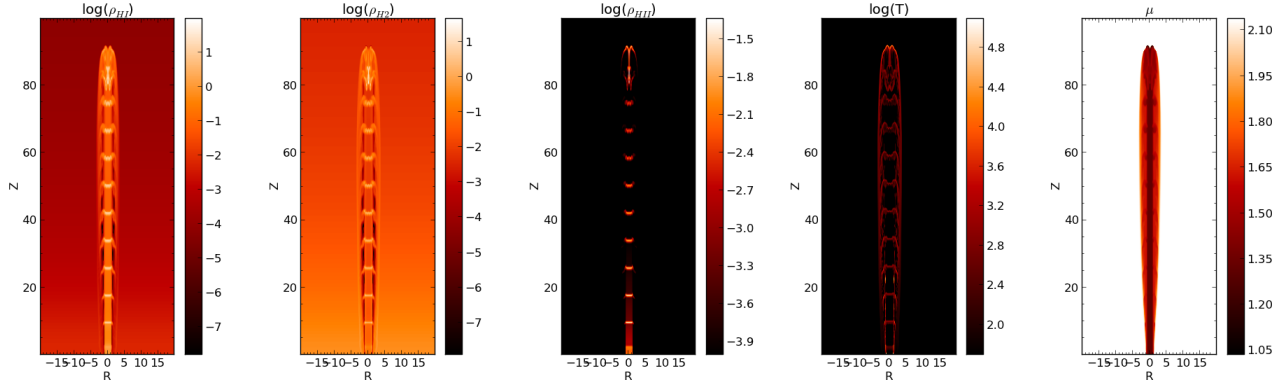
Figure 6. Fraction of hydrogen species in the run with molecular cooling having $\eta = 3$ and $\beta = 10$.
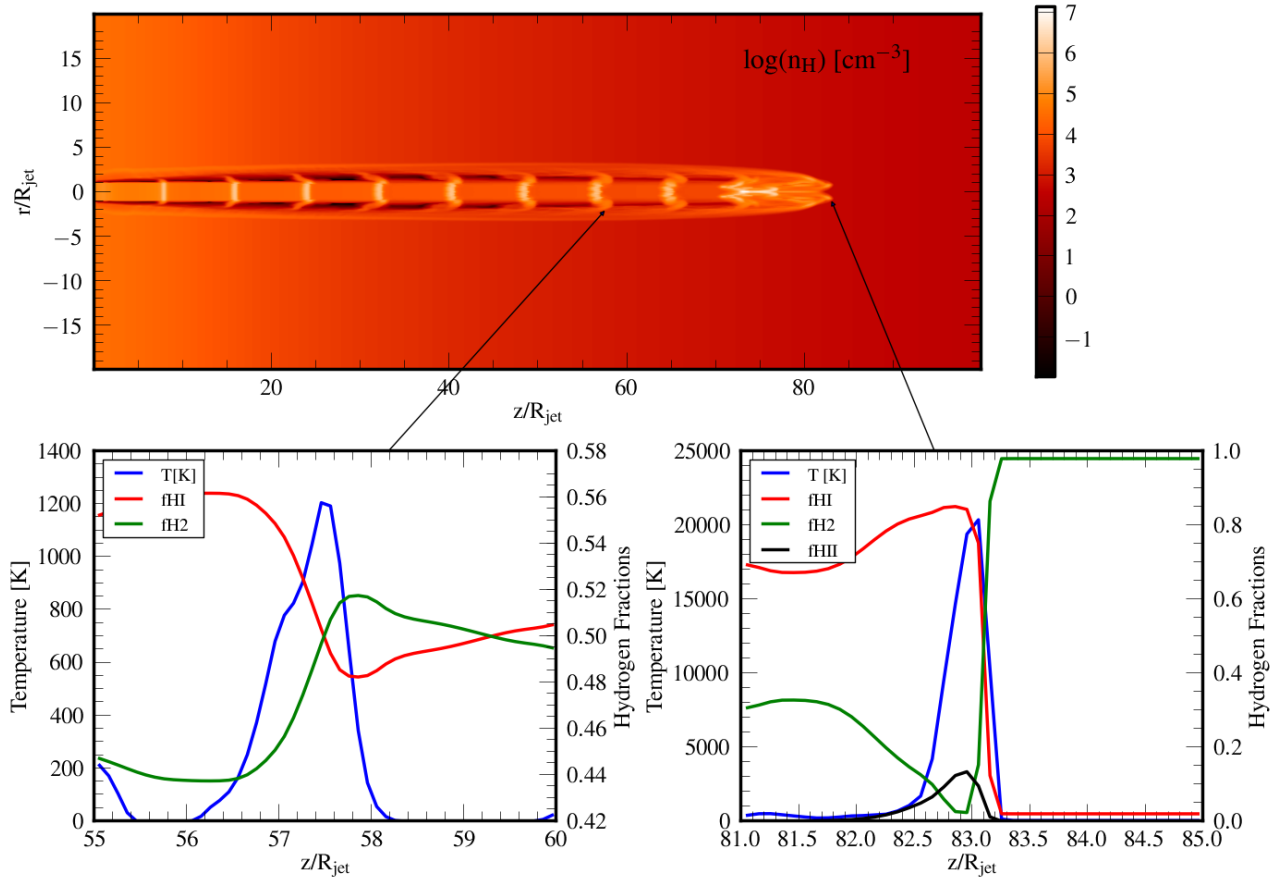
Figure 7. Dependence of hydrogen fractions on the temperature at two points in the flow, viz. the interface of the knot with molecular medium and at the bow shock

and region close to the bow shocks. They are marked by horizontal white dashed lines in the emission maps. The knot closer to the base is the brightest showing a peak intensity of 50 K. As one moves along the jet the intensity decreases and reaches to about 10 K close to the bow shock. The line widths seen for this reference run with an angle of inclination of 90° are typically around 5-10 km s^{-1}. These line widths increase substantially as the angle of inclination decreases. Figures 9 and 10 show the emission map, PV diagram and spectra for the same reference run but with angle of inclination of

60° and 45° respectively. The spectra for low inclination angles are much broader and have lower peak intensities at the same three positions in the flow (shown by three white dashed lines). The line widths now are typically of the order of 20 km s^{-1} and the peak intensity of the brightest knot is approximately 10 K. The PV diagrams in these runs are not longer symmetric, unlike the run with the jet in plane of the sky. Instead, they show a distinct *zig-zag* pattern at each of the knots and region close to the bow shock.

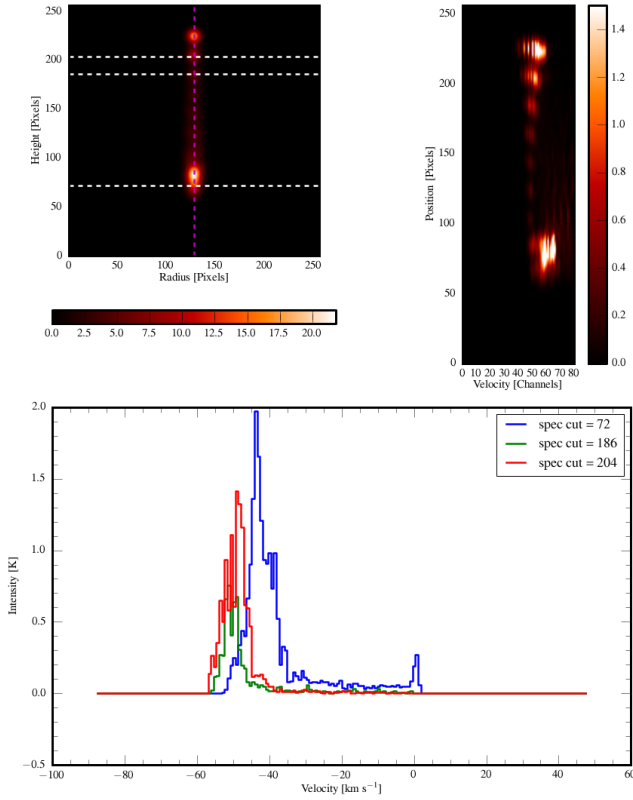The predicted emission maps, spectra and PV diagrams

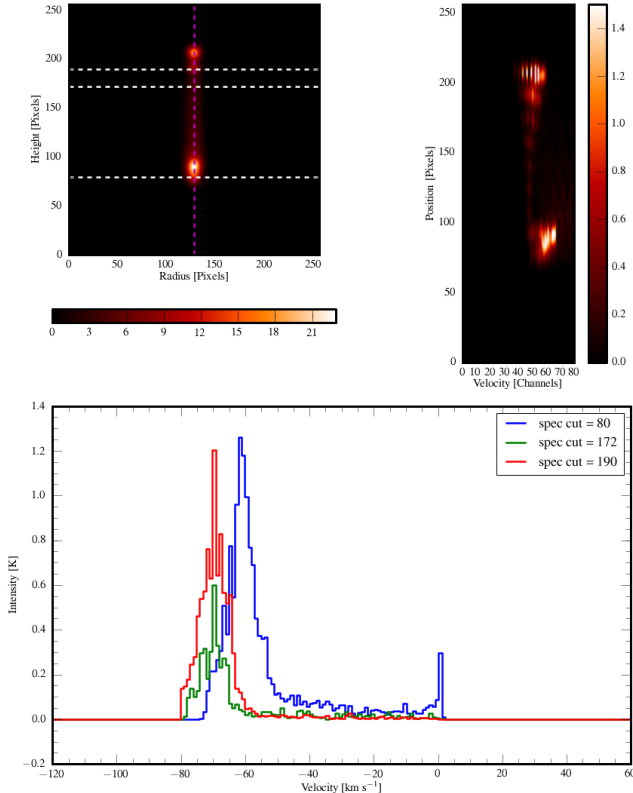**Figure 9.** Same as figure 8 but with angle of inclination of 60°.

Figure 10. Same as figure 8 but with angle of inclination of 45°.

are shown above to depend on the angle of inclination. In the next section, we focus on the dependence of these observational features on the different fractional abundance profiles of SiO.
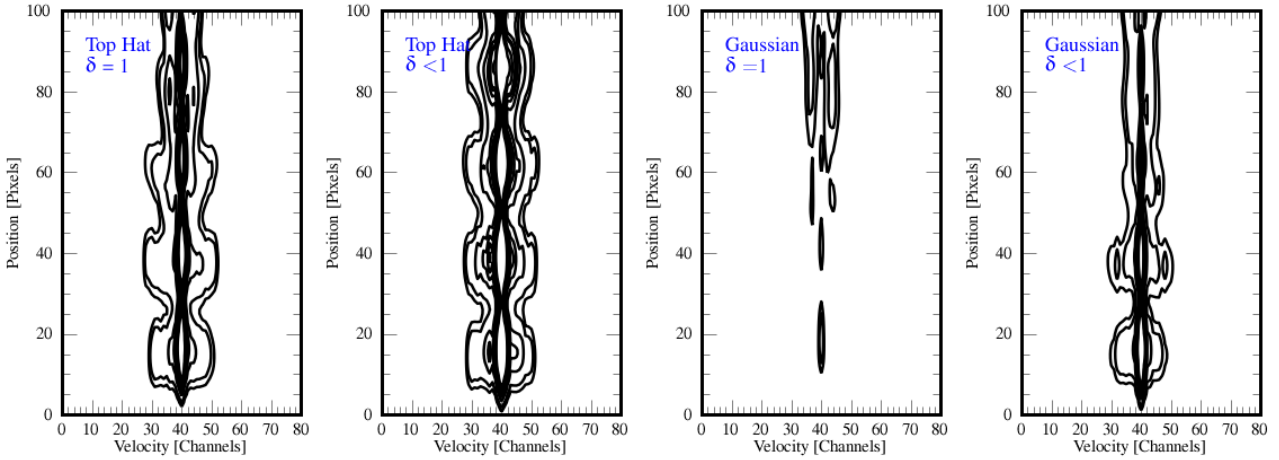
6.4   SiO Abundance profile

Input profiles in the radiative transfer code for the fractional abundance of SiO are a very modest approximation from observed values (see sec 4.3). In figure 11, we compare the maps for $J = 2\text{->}1$ emission for two different abundance profiles and ratio of jet to shock velocities. There is a striking difference with regards to emission from the internal knots in these images. All the internal knots show emission in the $J=2\text{->}1$ line whilst using a top hat profile and accounting for shock speeds (i.e. $\delta < 1$). However, some of these knots are not observed when using the same top-hat profile but assuming the shock velocity to be same as the jet velocity (i.e., $\delta = 1$). Similar qualitative characteristics are seen in case of a gaussian abundance profile. In particular, the case with $\delta = 1$ only produce emission from the knot closest to the bow shock, while the internal knots do not show any appreciable emission. Further, the emission from the knot closer to the bow shock varies considerably with different profiles and value of δ. It is the brightest for the case with a top-hat profile and $\delta < 1$. The peak emission and line widths at this knot are listed in table 3

The dependence of emission on SiO abundance profile is expected due to the distribution of jet velocity obtained from dynamical simulations. We see that the velocity of internal knots lie around $70\text{-}90 \, \text{km s}^{-1}$, while the pulsed jet was injected with a mean of $100 \, \text{km s}^{-1}$. The knots slow down during the evolutionary phase as they interact with the ambient medium. Interestingly, younger knots closer to the base of the jet are brighter compared to older ones further away from the jet (see panels 1 and 3 of fig 11). This is attributed to the fact that the ambient medium has a density gradient that goes as $\sim z^{-2}$. Thus, the younger knots suffer the most deceleration closer to the base of flow. This fact is taken into account when the shock velocity is consistently calculated using the density contrast and using a value of $\delta < 1$. This process is further validated by the lack of emission from internal knots in panel 4 of the fig 11.

Additionally, the internal knots show their distinct signatures in form of *Hubble wedges* as seen in the PV diagrams for these different profiles (see 6.3). Figure 12 shows a zoomed version of the bottom four internal knots in form PV diagram for these different abundance profile. As expected, the signatures of knotty emission is missing for the case with gaussian profile with $\delta = 1$. Further, the wedges formed in panels 1 and 2 of the figure in general slightly more extended in position space as compared to ones formed in panel 4 of the same figure. This is indeed because of the discontinuous nature of top-hat abundance profile as the SiO is enhanced to a maximum abundance for all velocities between 20 and 100 km s^{-1}, which is not the case in a more continuos gaussian distribution.
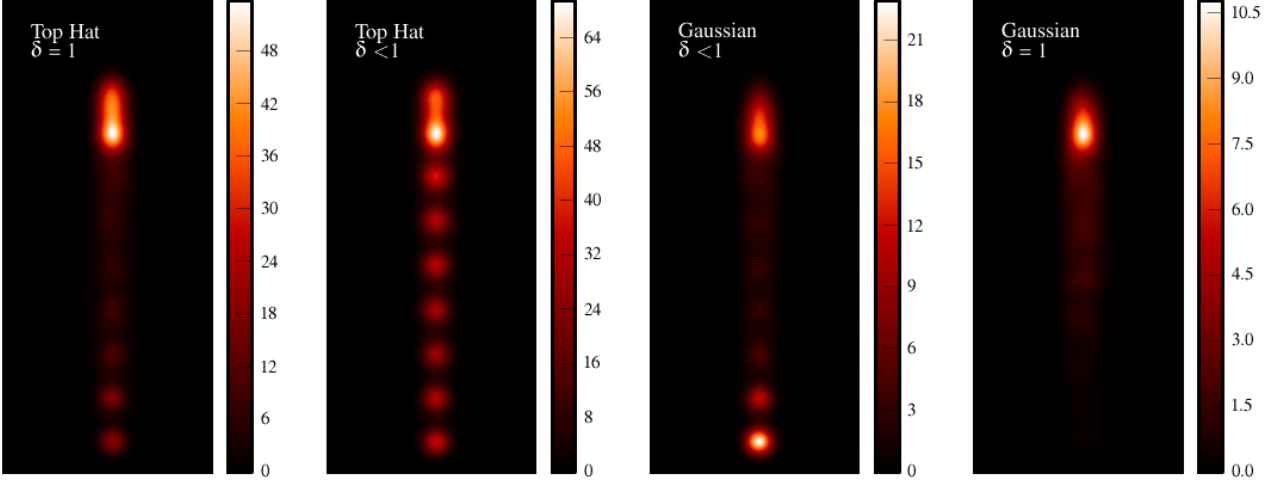
Figure 11. Variation of 2->1 SiO emission for runs with molecular cooling having $\eta = 3$ and $\beta = 10$ and different abundance profiles.

Figure 12. Contour maps of position-velocity diagram for the internal knots for 2->1 SiO emission for runs with molecular cooling having $\eta = 3$ and $\beta = 10$ and different abundance profiles. The contours mark different levels of emission in Kelvins, viz., 0.2,0.6,1.0,1.4,1.8,2.0,3.0,4.0.

7   ALMA VIEW

In order to see the interior structure of the molecular outflow, high resolution interferometric observations are needed. To demonstrate how jets similar to those we have modeled would look through such observations we have performed synthetic Atacama Large Millimeter Array (ALMA) observations using the Common Astronomy Software Applications package (CASA). The output from the radiative transfer were scaled to 300pc and used as the sky models for observations of the J=2-1, J=5-4 and J=8-7 lines at frequencies of 86.85, 217.10 and 347.33 GHz, which fall in ALMA bands 3, 6 and 7. The observations were simulated using cycle 1 ALMA for 30 minutes total integration time, in the configurations c32-6, c32-4 and c32-3 for the three lines, giving beam sizes of 0.72", 0.47" and 0.58" and sensitivities of 0.05, 0.07 and 0.09 mJy/beam for the three lines (as calculated by the ALMA online sensitivity calculator) with velocity resolutions of ~1 km/s. Figure 13 presents the AMLA prediction obtained from our reference run. The left panel shows the integrated emission of SiO J = 2-1 line while the

right shows the PV diagram for the same line and over laid are the contours of SiO J = 5-4 and J = 8-7. The contour levels are marked on the color bar of each panel.

ALMA Cycle 0 observations have recently reported complex kinematic features of young bipolar molecular outflows. In particular, Arce et al. (2013) observed morphology, kinematics and entrainment mechanism of the HH 46/47 molecular outflow from a low mass nearby source (d = 450 pc) using CO(1-0). They find that the red lobe of the outflow exhibits a very complex structure with a collimated episodic wind whereas the outflow in the blue lobe is consistent with wide-angle wind model. Three major clumps in the red lobe along the outflow axis show a distinctive signature in emission maps. In addition, these clumps appear as *wedges* in the PV diagram. The observed *wedges* are very similar in structure to that seen in the right panel of figure 13. A quantitative comparison is not possible due to obvious difference of molecular lines. Another source which is studied in details with ALMA band 7 is one of the most energetic, luminous molecular outflow G331.512-0.103 Merello
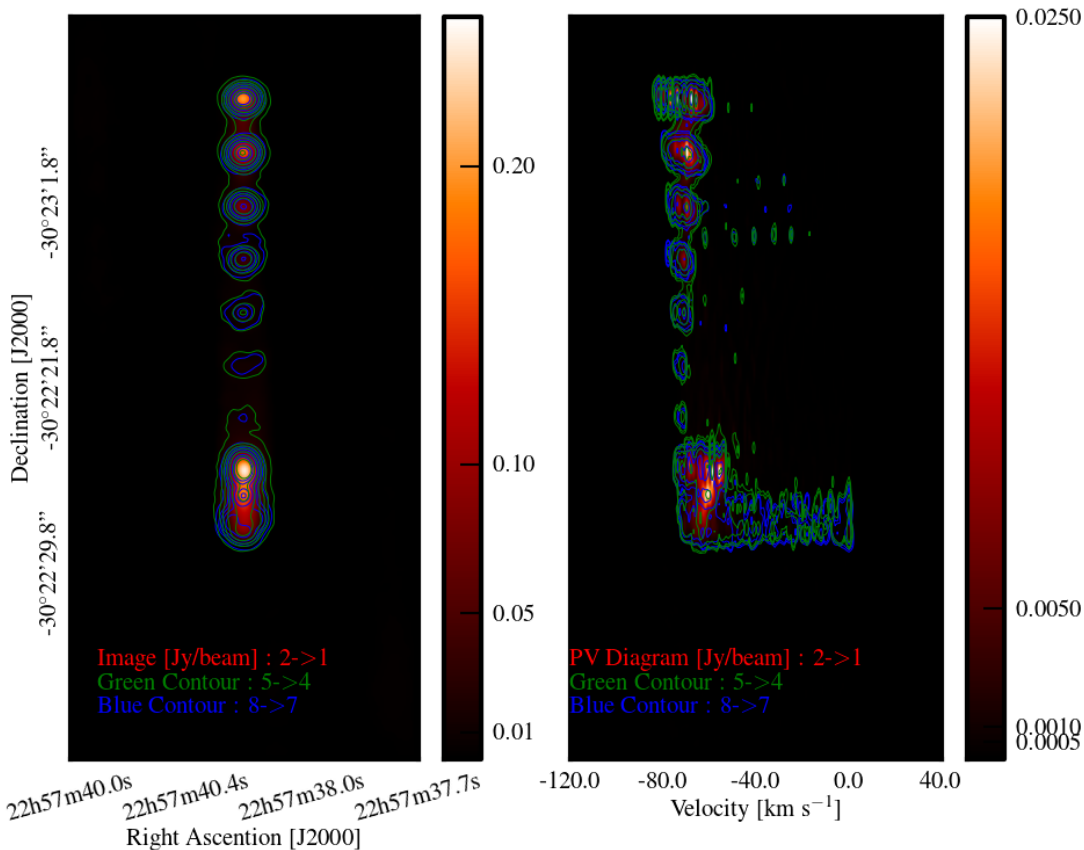
Figure 13. Left: The integrated intensity map of the three SiO lines simulated. The heat map shows the 5-4 line intensity (in units of $Jy\,kms^{-1}$/beam), the blue contours show the J=8-7 line intensity and the green contours show the J=2-1 line intensity. **Right:** The PV diagram taken along the axis of the jet (in units of Jy/beam), showing the higher J transitions highlighting the knots of the jet and broad emission at the bow shock. In both panels the ticks on the color bar represent the contour levels, the levels not shown on the integrated intensity color bar are double the previous level.

et al. (2013). Observations of this outflow associated with a high mass star reveal a compact, extremely young bipolar outflow and a symmetric outflowing shell. Further, their PV diagrams with SiO and $H^{13}CO^+$ show a characteristic peak at -45 $km\,s^{-1}$ along the primary axis that could associated with a molecular *bullet* of high-velocity dense material as predicted from our synthetic maps.

8 DISCUSSION

Here we compare the various results with SiO observation of young low mass and high mass outflows.

8.1 EHV component and Molecular bullets

Multiline mm-wavelength surveys of SiO emission towards a sample of molecular outflows have shown that these outflows exhibit both low and high velocity SiO emission possibly arising from two distinct regimes. The slow component in the case of a typical outflow, L1448, is believed to arise from the shell of accelerated ambient gas with SiO abundance lower by two orders of magnitude than regions emit-

ting the high velocity component. Codella et al. (1999). In addition, an interesting feature of EHV gas is seen in many young molecular outflows. The origin of EHV component is still a mystery, however, recent high resolution observations have tried to study the composition of such extremely high velocity gas Tafalla et al. (2010). Typically, EHV gas feature in high density gas tracers (like CO and SiO) and show significantly weak emission of $\sim 0.1\,K$.

In IRAS 04166+2706, Santiago-García et al. (2009) have shown that the EHV CO(2-1) emission is mapping a jet-like feature that runs along the middle and consists of a collection of discrete peaks. These peaks of EHV emission are placed located in a perfect symmetry on both sides of the outflow lobe. This symmetry indicate that such EHV peaks might arise from events that took place near the central source and have since propagated in the flow Bachiller et al. (1990); Tafalla & Bachiller (2011). The dynamical model in conjunction with proper radiative transfer calculations presented here agrees very well with the above scenario. The *bullets* in our work are injected into the flow in a sinusoidal manner along with a collimated atomic jet. These pulsating ejections do interact with the medium via shocks and exciting high velocity gas. Cooling associated with molecules

and tracing of H_2 chemistry with the flow allows us to consistently identify the regions where molecular hydrogen is formed and disassociated (see fig. 7). The SiO emission that we obtain from our radiative transfer calculations is associated with regions where shocked H_2 gas is present. A contour map of SiO emission obtain from the reference run is shown in figure 14. Such a model can very well explain the shocked SiO velocity components observed in L1157 molecular outflow Gueth et al. (1998).

Further, we find SiO emission coming from velocities of the order of 40-60 $km\,s^{-1}$ (see figs. 9 and 10). Such a velocity range is typically associated with EHV gas seen in majority of the outflows Tafalla & Bachiller (2011). Additionally, the EHV peaks show a distinct sawtooth pattern in the PV diagram Santiago-García et al. (2009). Such a sawtooth pattern is very similar to the pattern that we see in PV diagrams from our models (see figs. 9 and 10). All of the above striking similarities from observations of EHV gas and synthetic spectra and PV diagrams gives a very formidable backing to the idea that such an emission could arise due to shock interactions of internal knots in the flow. In the section below we further compare the line ratios and intensities from our results with single dish measurements of typical outflows with EHV emission.

8.2 Line transitions and ratio

Numerous molecular outflows with jet-like bullets have been observationally studied till date. In particular, H7-11 (Bachiller et al. 1998), IRAS 04166+2706 (Santiago-García et al. 2009; Tafalla et al. 2010), HH211 (Nisini et al. 2002) L1448 (Bachiller et al. 1991; Nisini et al. 2007; Tafalla et al. 2010) and L1157 (Nisini et al. 2007) have shown clear signatures of EHV component. Among them L1448, HH211 and L1157 have been studied in details using an extensive multi-line survey of SiO. Such a multi-frequency analysis helps to understand the dependence of excitation conditions for these lines on velocity, based on existing shock models.

Figure 14 show symmetrical contour maps of integrated emission convolved with a 2″ beam coming from different line transitions for our reference model. The most striking feature seen in that figure is the progressive shift of emitting region from the interface to internal knots with increase in excitation energies of different lines. In particular, the lowest transition J=1->0 shows most of the emission coming from the interface between the jet and ambient medium, along with emission from the dense knots formed at the base of the flow. While, emission coming due to high energy transitions, J=5->4 and 8->7, is more concentrated in the inner jet regions and arise mainly from the shocks due to internal knots. Such a trend in emission with excitation energies coming from different SiO line transitions have been observed in many young outflows (for e.g., *L1448* bullets (Nisini et al. 2007), *HH211* (Chandler & Richer 2001; Nisini et al. 2002; Hirano et al. 2006)). Further, the evolved post-shock gas near the primary bow shock also show bright emission for these high J transitions. This gas is linked to the Rayleigh-Taylor instability associated with cooling flows (see section 6.1). The sub-structure seen close to the primary bow shock with high resolution does give a sense of clumpiness in the flow backing the suggestions to explain clumpy SiO emission by Chandler & Richer 2001.

Nisini et al. (2007) have shown that the current plane-parallel shock models fit reasonably well the physical conditions traced by the SiO emission i.e., temperature $\lesssim 1000\,K$ and H_2 number density $\sim 10^5$-10^6 cm^{-3}. They can also fit the observed fractional SiO abundance of $\sim 10^{-7}$ in these outflows. However, they fail to predict all the line profiles and in particular their similarities for low and high excitation lines. Line emission for SiO from our model also traces similar physical environment. Fig 7 shows that regions close to the internal knot have temperatures up to $1000\,K$ and molecular hydrogen density of the order of 10^5 cm^{-3} about half that of the total hydrogen density in that region. These regions are where bulk of the SiO emission is obtained in our models. Additionally, the internal knots move with velocity of 70-90 $km\,s^{-1}$, indicating a fractional SiO abundance between 10^{-6} to 10^{-8}, depending on the choice of abundance profile (see fig 3). The line profile shapes obtained from this study fit reasonable well with that observed by Nisini et al. (2007), especially for the bullets seen in L1448. Interestingly, we see in our models, where we relax the plane parallel approximation, the line profiles are equally broadened for low as well as high excitation lines. The top panel of fig. 15 shows spectra for three line transitions for the reference run but with an angle of inclination, $\phi = 60°$ and convolved with a single dish beam of 15″. Additionally, the predicted integrated intensities also lie within a factor of two from the values of L1448 bullets observed with JCMT and IRAM (Table 2 of Nisini et al. 2007 and table 3 of this work).

The variation of integrated single dish emission with upper transition levels J_{up} for different abundance profiles is shown in the right panel of fig. 15. It is clear, that a emission obtained using a top hat profile is brighter as compared to one obtained with a gaussian profile, due to its obvious high estimate of SiO abundance in regions of interest. However, curves obtained from both these profiles show a very similar shape of a distinct rise followed by a fall in integrated emission for higher transitions with a peak in emission for $J_{up} = 3$. Similar profiles are also predicted and used to estimate the physical conditions assuming optically thin emission from LVG modeling for L1448 and L1157 Nisini et al. (2007). However, this usual approach did not give accurate results for line ratios SiO(8-7)/(5-4) and SiO(5-4)/(2-1) in case of HH212. Values ≈ 1 for both ratios were only achieved in optically thick LTE regime (Cabrit et al. 2007; Lee et al. 2008). Similar values are also obtained for molecular outflows from massive young stellar object IRAS 17233-3606 Leurini et al. (2013). These line ratios from the present non-LTE radiative transfer model are shown in the bottom left panel of fig. 15. Their values lie very close to unity as indicated from observations. Further, we have estimated the optical depth in regions emitting SiO and find them to be optically thick with an optical depth $\tau \sim 10$. Thus, assuming optically thin SiO emission from molecular outflows especially from shocked dense knots would only provide upper limits. In summary, the shape, ratio and peak intensity of the spectra obtained from our model fit very well to observed values implying that SiO emission from our model is tracing the regions with right physical conditions that are required to emit SiO in gas phase via shocks.
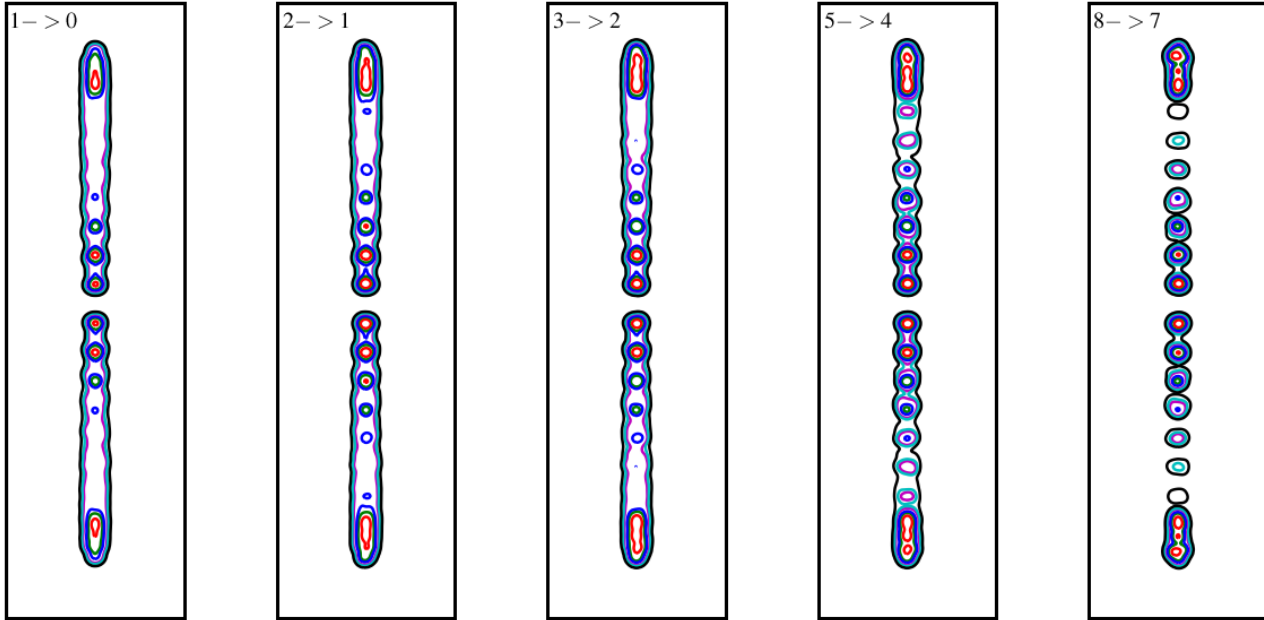
Figure 14. Contours of SiO emission for different line transitions obtained for the run with molecular cooling with $\eta = 3$ using the functional form of the SiO fractional abundance with $\delta < 1$. The contour colors represent different intensities in Kelvins, i.e, $30.0(red)$, $10.0(green)$, $5.0(blue)$, $1.0(magenta)$, $0.5(cyan)$, $0.1(black)$.

8.3   Slow Component and Grain Chemistry

We have presented a formidable model to explain the EHV component seen in SiO emission from several young outflows. The reference model consistently solves for the H_2 chemistry in presence of appropriate cooling. The steady state temperature, density and velocities obtained from dynamical simulation is post-processed to obtain SiO maps, spectra and PV diagrams. One essential ingredient required for the radiative transfer modeling is the SiO fractional abundance and its dependence on shock velocity. Though 1D models that study the formation of SiO in gas phase from grain-grain and grain-mantle collisions exists, their focus is mainly on weaker shocks Schilke et al. (1997); Caselli et al. (1997); Gusdorf et al. (2008). The pulsating jet propagation model presented here have shock speeds reaching up to 100 km s^{-1}. For simplicity we have used two basic prescription of SiO abundance profile as a function of shock velocity. Though the shape of the profile is uncertain the upper and lower limits used are backed by observational evidences. Ideally for a consistent dependence of SiO abundance on shock velocity, one would have to also solve for silicon and SiO chemistry in a manner similar to that of H_2. Further by evolving the dynamical simulations with complex grain chemistry for more than 10^4 years (time to destroy SiO in gas phase Codella et al. (1999)), one can trace the history of SiO in molecular outflows. However, such a numerically expensive model with complex chemistry is beyond the scope of this paper.

The model presented in this paper target the very early phase of molecular outflows i.e., dynamical time scale of 1000 years. As discussed in sections above, the unique combination of pulsating jet with chemistry and cooling followed by non-LTE radiative transfer calculations has shown success in fitting the line shapes, integrated intensity and line ratios of SiO transitions arising from EHV gas. However, the synthetic spectra show no signatures of slow SiO component that accompanies EHV emission seen in many outflows. The physical mechanism for the origin of slow SiO component is still a matter of debate. One of the suggestion is it arises due to slowing down of shocked gas as they age. The time scale estimated for the shocked gas to slow down is of the same order of magnitude as the SiO destruction time scale i.e., 10^4 years Codella et al. (1999). In this case, we will not be able to see the effect as the dynamical runs do not evolve beyond 10^3 years. However, we do see initial hints of slowing down of more evolved gas in terms of the velocity shift of about 7-10 km s^{-1} in peak emission between that coming from the freshly formed internal knots close to the base of the flow as compared to emission coming from more evolved gas near the primary bow shock. To ascertain this fact in more details, one would need to track the primary bow shock for 10^4 years using a larger simulation box and possibly with adaptive gridding which will be considered for future simulations. Such a long term evolution will also help to provide a numerical model for the formation of HH objects which are believed to be slowed down and more evolved form of these young molecular bullets as suggested by Norman & Silk (1979); Hartigan et al. (1987).

An alternative hypothesis for the origin of the low velocity SiO component is that it could be formed by interaction of wider slow shocks with the ambient medium. Generally it is assumed that the silicon material comes from dust grain cores and that it is necessary to fully destroy the dust grains to obtain some SiO in gas phase. However, some silicon material may be mixed with the ices on the dust grain surfaces. In such a scenario, shocks with speeds of 20-30 km s^{-1} might inject a significant amount of silicon into the gas phase from the mantles, without completely destroying the grains. Testing such a scenario is beyond the scope of the present model.
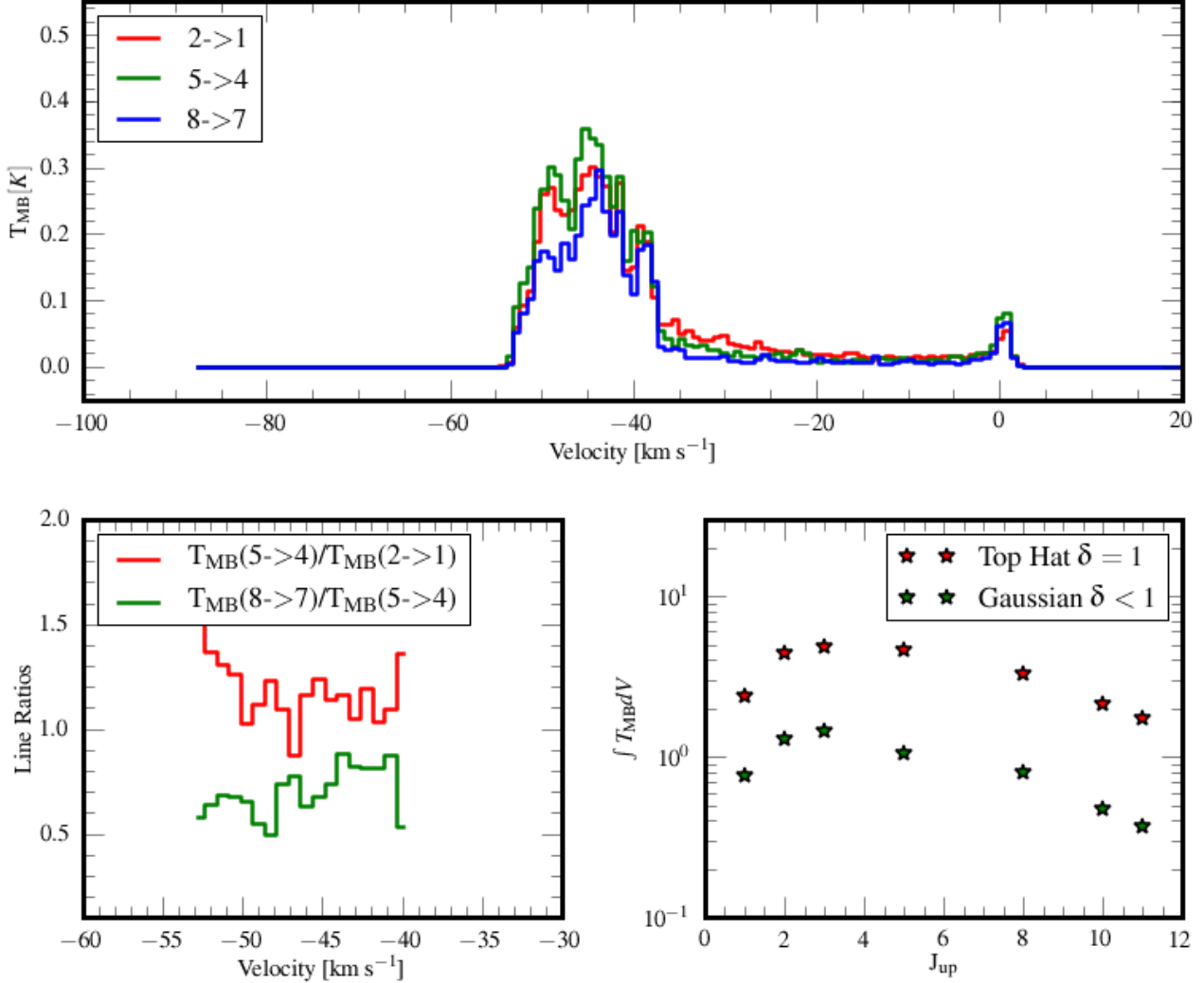
Figure 15. *Top* Line profiles in SiO J = 2-1, 5-4 and 8-7 at one the inner knot for the molecular cooling run with $\eta = 3$ and $\beta = 10$ using top hat abundance profile with $\delta = 1$. The profiles are obtained when the angle of inclination is 60° with respect to line of sight. *Bottom left* Line intensity ratios SiO(8-7)/(5-4) and SiO(5-4)/(2-1), as a function of velocity. *Bottom right* Variation of integrated intensity with upper line transition J_{up} for two abundance profiles.

One would not only need proper treatment of dust physics but also a two fluid model to study the impact of slow shocks in two dimensions. These models are indeed very important to study wide and slow emission from molecules like CO as seen in some young outflows like L1157 Gómez-Ruiz et al. (2013) and H_2O as seen from recent results of the Herschel-WISH survey Tafalla et al. (2013).

9   CONCLUSION

We have performed MHD simulations of interaction of knotty and radiative jet propagating with a typical speed of 100 km s^{-1} into a cold, non-magnetized ambient molecular medium a density gradient. At large distance from the central source, the magnetic field in the jet is mainly due to toroidal component. The jet dynamical quantities are evolved in conjunction with different optically thin, non-equilibrium cooling prescriptions of varying complexities. The most complex is that of molecular cooling along with

H_2 chemistry. This prescription allows us to track the formation and destruction of HI, HII and H_2 along with the flow dynamics. The final state of the jet obtained for each cooling model is then post-processed using a radiative line transfer code to obtain SiO emission maps, spectra and PV digrams. The main results obtained from our study are as follows :

• Different cooling prescriptions used for our model show a significant influence in determine the thickness of the jet. An efficient mode of cooling does reduce the size of cocoon and results in a more narrow jet. In addition, the primary bow shock structure differs with various cooling modes. Also, with realistic cooling functions one sees development of thermal instability at the jet head which also show a significant emission in SiO along with young internal knots that are formed close to the base of the jet.

• Emission maps obtained from our reference run with molecular cooling show a distinctive outflow lobe like structure. The physical regions responsible of SiO emission in

such early outflows typically have molecular hydrogen densities n$\sim 10^6$ cm^{-3} and temperatures $> 500\,$K which is consistent with properties deduced from LVG modeling of real observational data of young outflows.

• Our multi-line study of SiO clearly shows how different line transitions are sensitive to different regions in the jets. For example, the SiO J = 1-> 0 transition is mostly excited due to interaction of jet with ambient medium and could possibly be turbulent, while SiO J = 8-> 7 trace the inner most jet regions as they are excited only in the internal knots. This finding very well supports the multi-line observational surveys done for young molecular outflows, particularly, HH 211.

• Single-dish synthetic spectra obtained from our model typically have intensity of $0.3\,$K and peak around $50\,$km s^{-1} and have a typical line width of $20\,$km s^{-1}. Such modeled spectra are in excellent agreement with characteristic features of EHV emission of SiO seen in young molecular outflows . In addition, the line ratios T(8-7)/T(5-4) and T(5-4)/T(2-1), predicted from our models have values close to unity consistent with that obtained from observations. Further, indications of formation of slow component due to slowing of the older knots is clearly seen as a shift in spectra by 8-10 km s^{-1} in first 10^3 years of evolution.

• The predicted PV diagrams from our models show a distinctive knot like features that are generally observed in outflows with EHV emission.

• Emission from internal knots do depend on the chosen profile of the abundance. On one extreme where all the internal knots is the top-hat profile with $\delta < 1$, whereas, no emission in seen in knots when a gaussian profile with $\delta = 1$ is used. For the remaining two possibilities, we observe that emission mainly comes from knots close to the base of the flow and the condensation formed at the primary shock due to thermal instability.

• Predicted ALMA maps also show characteristic features that are consistent with young molecular outflows with EHV emission.

In summary, this work for the first time provides a formidable model that explains the origin of EHV emission seen in SiO from the inner regions of young molecular outflows.

REFERENCES

Abel T., Anninos P., Zhang Y., Norman M. L., 1997, New A, 2, 181

Arce H. G., Goodman A. A., 2001a, ApJ, 554, 132

Arce H. G., Goodman A. A., 2001b, ApJ, 551, L171

Arce H. G., Mardones D., Corder S. A., Garay G., Noriega-Crespo A., Raga A. C., 2013, ApJ, 774, 39

Arce H. G., Shepherd D., Gueth F., Lee C.-F., Bachiller R., Rosen A., Beuther H., 2007, Protostars and Planets V, pp 245–260

Bacciotti F., Ray T. P., Mundt R., Eislöffel J., Solf J., 2002, ApJ, 576, 222

Bachiller R., 1996, ARA&A, 34, 111

Bachiller R., Guilloteau S., Gueth F., Tafalla M., Dutrey A., Codella C., Castets A., 1998, A&A, 339, L49

Bachiller R., Martin-Pintado J., Fuente A., 1991, A&A, 243, L21

Bachiller R., Martin-Pintado J., Tafalla M., Cernicharo J., Lazareff B., 1990, A&A, 231, 174

Beuther H., Schilke P., Gueth F., McCaughrean M., Andersen M., Sridharan T. K., Menten K. M., 2002, A&A, 387, 931

Blandford R. D., Payne D. G., 1982, MNRAS, 199, 883

Blondin J. M., Fryxell B. A., Konigl A., 1990, ApJ, 360, 370

Brinch C., Hogerheijde M. R., 2010, A&A, 523, A25

Cabrit S., Bertout C., 1992, A&A, 261, 274

Cabrit S., Codella C., Gueth F., Nisini B., Gusdorf A., Dougados C., Bacciotti F., 2007, A&A, 468, L29

Canto J., Raga A. C., 1991, ApJ, 372, 646

Caselli P., 2011, in Cernicharo J., Bachiller R., eds, IAU Symposium Vol. 280 of IAU Symposium, Observational Studies of Pre-Stellar Cores and Infrared Dark Clouds. pp 19–32

Caselli P., Hartquist T. W., Havnes O., 1997, A&A, 322, 296

Cen R., 1992, ApJS, 78, 341

Cerqueira A. H., de Gouveia dal Pino E. M., 1999, ApJ, 510, 828

Chandler C. J., Richer J. S., 2001, ApJ, 555, 139

Codella C., Bachiller R., Reipurth B., 1999, A&A, 343, 585

Downes T. P., Cabrit S., 2003, A&A, 403, 135

Dutrey A., Guilloteau S., Bachiller R., 1997, A&A, 325, 758

Flower D. R., Le Bourlot J., Pineau des Forêts G., Cabrit S., 2003, MNRAS, 341, 70

Galli D., Palla F., 1998, A&A, 335, 403

Glassgold A. E., Mamon G. A., Huggins P. J., 1991, ApJ, 373, 254

Goddi C., Greenhill L. J., Chandler C. J., Humphreys E. M. L., Matthews L. D., Gray M. D., 2009, ApJ, 698, 1165

Gómez-Ruiz A. I., Hirano N., Leurini S., Liu S.-Y., 2013, ArXiv e-prints

Gueth F., Guilloteau S., 1999, A&A, 343, 571

Gueth F., Guilloteau S., Bachiller R., 1998, A&A, 333, 287

Guillet V., Jones A. P., Pineau Des Forêts G., 2009, A&A, 497, 145

Gusdorf A., Cabrit S., Flower D. R., Pineau Des Forêts G., 2008, A&A, 482, 809

Hartigan P., Raymond J., Hartmann L., 1987, ApJ, 316, 323

Hirano N., Liu S.-Y., Shang H., Ho P. T. P., Huang H.-C., Kuan Y.-J., McCaughrean M. J., Zhang Q., 2006, ApJ, 636, L141

Hollenbach D., McKee C. F., 1979, ApJS, 41, 555

Konigl A., Pudritz R. E., 2000, Protostars and Planets IV, p. 759

Lee C.-F., Ho P. T. P., Bourke T. L., Hirano N., Shang H., Zhang Q., 2008, ApJ, 685, 1026

Leurini S., Codella C., Gusdorf A., Zapata L., Gómez-Ruiz A., Testi L., Pillai T., 2013, A&A, 554, A35

Lloyd S., 1982, Information Theory, IEEE Transactions on, 28, 129

Martin-Pintado J., Bachiller R., Fuente A., 1992, A&A, 254, 315

Masson C. R., Chernin L. M., 1992, ApJ, 387, L47

Masson C. R., Chernin L. M., 1993, ApJ, 414, 230

Merello M., Bronfman L., Garay G., Lo N., Evans II N. J.,

Nyman L.-Å., Cortés J. R., Cunningham M. R., 2013, ApJ, 774, L7

Mignone A., Bodo G., Massaglia S., Matsakos T., Tesileanu O., Zanni C., Ferrari A., 2007, ApJS, 170, 228

Neufeld D. A., Dalgarno A., 1989a, ApJ, 340, 869

Neufeld D. A., Dalgarno A., 1989b, ApJ, 344, 251

Nisini B., Codella C., Giannini T., Richer J. S., 2002, A&A, 395, L25

Nisini B., Codella C., Giannini T., Santiago Garcia J., Richer J. S., Bachiller R., Tafalla M., 2007, A&A, 462, 163

Norman C., Silk J., 1979, ApJ, 228, 197

Offner S. S. R., Lee E. J., Goodman A. A., Arce H., 2011, ApJ, 743, 91

Panoglou D., Cabrit S., Pineau Des Forêts G., Garcia P. J. V., Ferreira J., Casse F., 2012, A&A, 538, A2

Powell K. G., Roe P. L., Linde T. J., Gombosi T. I., de Zeeuw D. L., 1999, Journal of Computational Physics, 154, 284

Raga A., Cabrit S., 1993, A&A, 278, 267

Raga A. C., Taylor S. D., Cabrit S., Biro S., 1995, A&A, 296, 833

Rawlings J. M. C., Redman M. P., Carolan P. B., 2013, MNRAS, 435, 289

Santiago-García J., Tafalla M., Johnstone D., Bachiller R., 2009, A&A, 495, 169

Schilke P., Walmsley C. M., Pineau des Forets G., Flower D. R., 1997, A&A, 321, 293

Shang H., Allen A., Li Z.-Y., Liu C.-F., Chou M.-Y., Anderson J., 2006, ApJ, 649, 845

Shu F. H., Ruden S. P., Lada C. J., Lizano S., 1991, ApJ, 370, L31

Smith M. D., Rosen A., 2003, MNRAS, 339, 133

Stone J. M., Hardee P. E., 2000, ApJ, 540, 192

Tafalla M., Bachiller R., 2011, in Cernicharo J., Bachiller R., eds, IAU Symposium Vol. 280 of IAU Symposium, Molecules in Bipolar Outflows. pp 88–102

Tafalla M., Liseau R., Nisini B., Bachiller R., Santiago-García J., van Dishoeck E. F., Kristensen L. E., Herczeg G. J., Yıldız U. A., 2013, A&A, 551, A116

Tafalla M., Santiago-García J., Hacar A., Bachiller R., 2010, A&A, 522, A91

Vaidya B., Fendt C., Beuther H., Porth O., 2011, ApJ, 742, 56

Vaidya B., Goddi C., 2013, MNRAS, 429, L50

Woodall J., Agúndez M., Markwick-Kemper A. J., Millar T. J., 2007, A&A, 466, 1197

Ziurys L. M., Friberg P., Irvine W. M., 1989, ApJ, 343, 201